

# Bimodal ultrasound and fluorescence approach for prostate cancer diagnosis

**Jerome Boutet**  
**Lionel Herve**  
**Mathieu Debourdeau**  
**Laurent Guyon**  
**Philippe Peltie**  
**Jean-Marc Dinten**

CEA-LETI-MINATEC French Atomic Energy  
Comission  
17 rue des Martyrs  
Grenoble, F38054  
France

**Laurent Saroul**  
**Francois Duboeuf**  
**Didier Vray**

CREATIS INSA Lyon National Institute for  
Applied Sciences  
Batiment Blaise Pascal  
7 Avenue Jean Capelle  
Villeurbanne, 69621  
France

**Abstract.** Finding a way to combine ultrasound and fluorescence optical imaging on an endorectal probe may improve early detection of prostate cancer. The ultrasound provides morphological information about the prostate, while the optical system detects and locates fluorophore-marked tumors. A tissue-mimicking phantom, which is representative of prostate tissues both on its optical (absorption  $\mu_a$  and diffusion  $\mu'_s$ ) and its ultrasound properties, has been made by our team. A transectal probe adapted to fluorescence diffuse optical tomography measurements was also developed. Measurements were taken on the prostate phantom with this probe based on a pulsed laser and a time-resolved detection system. A reconstruction algorithm was then used to help locate and quantify fluorescent inclusions of different concentrations at fixed depths. © 2009 Society of Photo-Optical Instrumentation Engineers. [DOI: 10.1117/1.3257236]

Keywords: prostate; cancer; diagnostic; fluorescence; optics; ultrasounds.

Paper 08380RR received Oct. 22, 2008; revised manuscript received May 26, 2009; accepted for publication Sep. 8, 2009; published online Nov. 12, 2009.

## 1 Introduction

Prostate cancer diagnosis is based on prostate specific antigen (PSA) dosage and digital rectal examination. If the test is positive, a biopsy is conducted and guided by ultrasound imaging. However, current ultrasound imaging techniques are unable to detect tumors of small and medium size, and biopsies are performed in the prostate by following a systematic sampling pattern. This pattern covers the areas having the highest rates of cancer occurrence but some tumors may nonetheless remain undetected. Consequently, the only way to improve detection is to increase the number of biopsies. But this number cannot be increased because it may lead to major complications (6.6% of patients) such as acute prostatitis (3.8%), acute urinary retention (2.1%), hematuria (1.9%), rectal bleeding (0.2%), epididymitis (0.2%), sepsis (0.05%), and vasovagal syncope (0.05%).<sup>1</sup> Finding a way to guide biopsies to tumors may decrease the rate of false negative cases and improve patient well-being.

Bimodal optical and ultrasound methods have already been proposed to solve this problem. The combined use of these complementary methods seems promising: ultrasound provides morphological information and optical detection may guide the biopsy needle to the tumor. As ultrasound probes are used in routine examinations, the addition of optics would not involve a drastic change in the clinical protocol, but would facilitate the penetration of this technology. Moreover, optical detection can be easily integrated in an ultrasound probe through the use of optical fibers. Last, the morphological in-

formation provided by ultrasound could be used to improve optical location of tumors, as shown in a simulation performed by Xu et al.<sup>2</sup>

To discriminate between cancerous and healthy tissues, some authors used the fact that tumors are more vascularized than the surrounding tissues to measure attenuation of the near-infrared (NIR) light.<sup>3</sup> Optical characteristics (absorption and diffusion) of healthy and cancerous prostates were clinically measured.<sup>4</sup> In order to design an optimized optical probe, simulations were conducted to evaluate the best distribution of optical fibers.<sup>5</sup> A bimodal endorectal probe combining ultrasound and optical measurements, based on NIR absorption by intrinsic or endogenous chromophores, was proposed and successfully tested in preclinical trials on canine prostates with venereal tumors.<sup>6</sup> Nevertheless, all of these methods are based on the intrinsic or endogenous contrast between tumoral and healthy tissues. Actually, to detect cancer cells at an early stage, a stronger contrast between cancerous and healthy cells is required. Agarwal et al.<sup>7</sup> proposed enhancing the contrast by means of optoacoustic measurements on specifically functionalized gold nanoparticles which also act as thermotherapy agents.

Using fluorescence for *in vivo* prostate cancer diagnosis seems to be another promising way to improve the specificity of detection. However, the time involved in developing these methods was lengthened by the absence of specific fluorescent markers. In 2008, Pu et al.<sup>8</sup> showed the efficacy of Cytate, a fluorescence marker derivative of Indocyanine Green (ICG), which conjugates to receptors on prostate cancer cells.

Although fluorescence has a huge potential to improve the specificity of detection, it has to contend with weaker signals

Address correspondence to: Jerome Boutet, CEA-LETI-MINATEC, Département des Micro-Technologies pour la Biologie et la Santé, 17 rue des Martyrs, Grenoble, F38054 France. Tel: 33-4-38-78-38-57; Fax: 33-4-38-78-57-87; E-mail: jerome.boutet@cea.fr

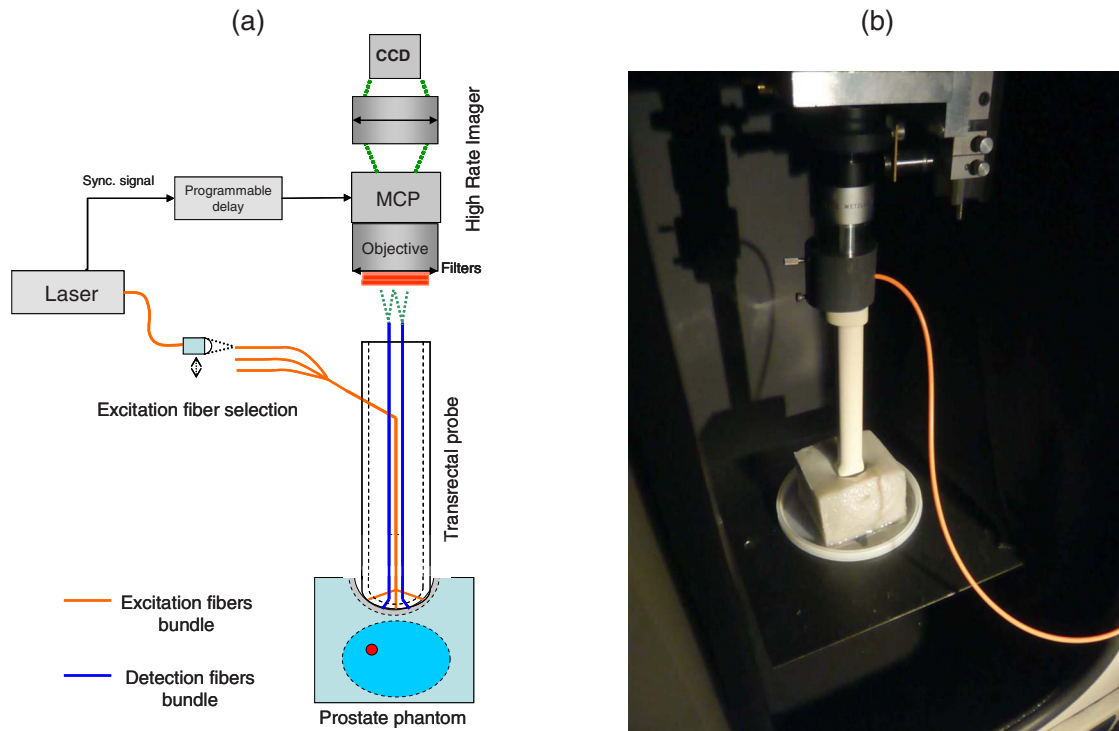


**Fig. 1** (a) Diagram of the time-resolved optical system. For simplicity's sake, only three out of six excitation fibers and two out of four-detection fibers are represented. (b) Photo of the optical transrectal probe gently pressed against the prostate phantom. The fluorescing inclusion is located 1.2 cm below the surface of the phantom.

than in NIR absorption measurements. This drawback implies the need for a high-power laser source and time-resolved detectors to locate the origins of fluorescence emissions more accurately. Fluorescence diffuse optical tomography (FDOT) techniques were successfully applied to the detection of tumors in small animals,<sup>9</sup> enabling imaging through a greater thickness of breast tissue ( $< 1.5$  cm). The small-animal approach of FDOT was even applied to human breast cancer<sup>10</sup> thanks to the weak light absorption coefficient of breasts ( $\mu_a \approx 0.03 \text{ cm}^{-1}$ ), which compensates for the greater thickness (5 to 9 cm).

Applying these techniques to prostate cancer diagnosis is a real challenge given that the absorption coefficient of prostatic tissues is very high ( $\mu_a \approx 0.3 \text{ cm}^{-1}$ ; Ref. 4), with a diffusion coefficient equivalent to lungs of small animals ( $\mu'_s \approx 7 \text{ cm}^{-1}$ ). Moreover, the geometry of an endorectal cavity is very confined, thus limiting us to reflection measurements that generate a high level of background signal noise (autofluorescence).

This article describes the first transrectal probe based on time-resolved FDOT. This probe was used to take measurements on fluorescent inclusions of various concentrations and located at fixed depths inside the prostate phantom. A reconstruction algorithm based on time-of-flight analysis was used to locate these inclusions accurately. Linearity experiments were also performed. Last, the system resolution was evaluated through simulation and the results discussed.

## 2 Materials and Methods

### 2.1 Description of the Optical and Ultrasound System

The schematic diagram of the optical system is illustrated in Fig. 1. It consists mainly of a pulsed titanium-sapphire laser, a transrectal optical probe, and a high rate imager (HRI). The laser (Spectra-Physics) was tuned to produce 50-fs pulses at 770 nm and 80-MHz frequency. The average laser power (10 mW) provides enough energy to penetrate deeply inside the phantom and to excite the inclusion. Its wavelength was chosen to fit the absorption peak of the fluorescing inclusion. The laser is filtered through a 770-nm bandpass filter (Thorlabs FB770). The excitation fiber selection is performed by a magnifying lens (Zeiss 10 $\times$  NA: 0.2) mounted on a displacement plate and moved in front of the desired fiber. The excitation fiber bundle is composed of six standard 62.5- $\mu\text{m}$ -diam silica fibers.

Figure 2 shows the drawings of the optical probe. Its dimensions are 15  $\times$  2 cm<sup>2</sup>. The axial ultrasound imaging transducer is located at the outer end of the probe. Both excitation and emission fibers are housed between the plastic shell of the probe and the transducer electronics. The optical head consists of 10 channels of fibers, 6 for excitation and 4 for fluorescence detection. The minimum source-detector separation distance of 10 mm ensures a good compromise between fluorescence intensity collection and background signal reduction. The emission fiber bundle is composed of four plastic high-aperture fibers (inner diameter=1 mm, NA=0.46, length

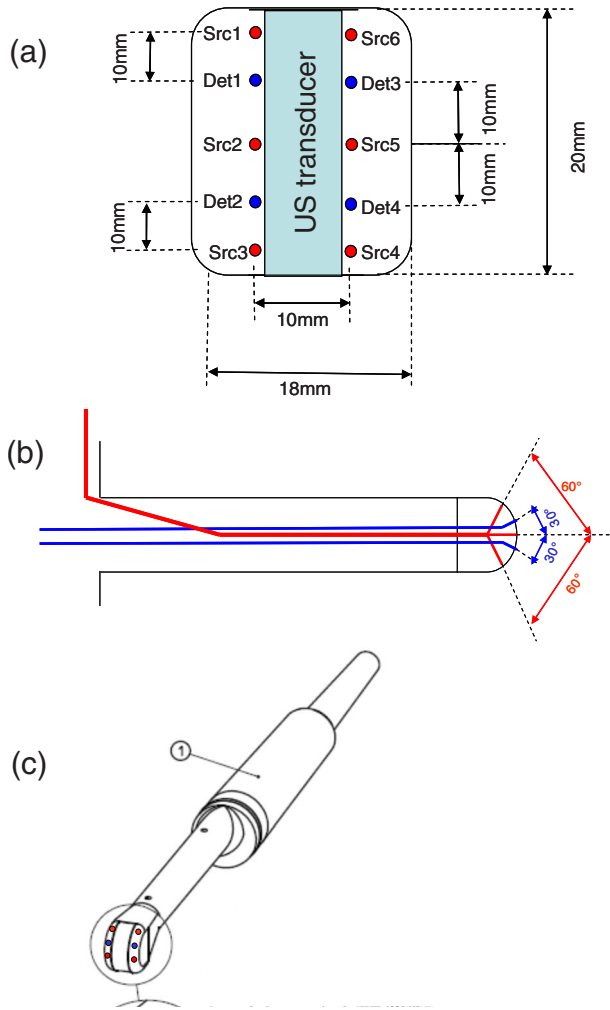


**Fig. 2** Diagram of the transrectal probe. (a) Front view of the bimodal optical head, with source and detector indexes. (b) Side view of the transrectal probe showing optical fiber angles. (c) Perspective view of the probe with handle (1).

=0.15 m) to optimize fluorescence collection. The signals from the four detection fibers are collected by a macrolens (Zeiss 6.3 $\times$ ). To handle the high level of excitation of the signal collected by the detection fiber, both Notch and Razor-edge filters were used (NF01-785U-25 and LP02-785RS-25 Semrock)

The fluorescence is detected by an intensified high-rate imager (Kentech). Inside the HRI, the photons are changed into electrons by a photocathode and amplified by a multi-channel plate (MCP). The photons generated by the phosphorous screen are focused and acquired by a 12-bit cooled CCD camera (Hamamatsu Orca-ER). An electronic gating system drives the high voltage of the MCP for time intervals of 300 ps. The time-dependent distribution of the fluorescence signal was measured by the use of a programmable delay system (Kentech).

To illustrate the feasibility of bimodal detection, auxiliary values were collected by combining time-resolved fluorescence and ultrasonic measurements. These experiments were not carried out with the transrectal probe but with a commercial system-[Ultrasonic 500RP by Ultrasonix Medical Corpo-

ration; Fig. 3(d)], which gives a planar view of the prostate phantom and can be displaced above the phantom in a more convenient way than a transrectal probe. The ultrasound system is mounted on a displacement table and acquires one planar image every 1 mm, in order to obtain a 3-D image of the prostate phantom. The ultrasound probe is positioned above the phantom, and several 1-mm-spaced transverse scans are acquired. The acoustic probe has a 6.7-MHz central frequency. The acoustic beam is focused near the central part of the phantom. Optical measurements were taken with the same laser and detection system but without excitation and detection fiber networks and in planar geometry. This work was previously described in Ref. 11. After this bimodal acquisition, the optical and ultrasonic slices are superimposed by means of standard image processing software.

## 2.2 Acquisition Parameters

In this feasibility study, the excitation light source is injected successively into the six excitation fibers. For each position of the laser, 68 images of the detection fibers are acquired with a time delay varying between 6 and 10 ns (in 0.025-ns steps). The MCP voltage is 830 V, and the exposure time of the camera 0.5 s. The overall acquisition time was 8 min. After scanning, the stack of images is stored on the hard disk with all the scanning parameters (source index, exposure time of each image, time delay). This stack is then used by the reconstruction algorithm to locate the fluorescent inclusion.

## 2.3 Inclusion Locating Method

The reconstruction principle is based on the model of the diffusion equation. For each excitation fiber  $s$ , the time-dependent distribution of the fluorescence intensity  $I_{sd}^F(t)$  detected by the fiber  $d$ , in the presence of the inclusion and the background signal  $I_{sd}^B(t)$  without the inclusion, are measured. The fluorescence signal  $I_{sd}(t) = I_{sd}^F(t) - I_{sd}^B(t)$  emitted by the inclusion and the first and second moments of this signal are calculated:

$$M_{sd}^0 = \int_0^{\infty} I_{sd}(t) \cdot dt, \quad (1)$$

$$M_{sd}^1 = \int_0^{\infty} I_{sd}(t) \cdot t \cdot dt, \quad (2)$$

where  $M^0$  is the total fluorescence intensity, and  $M^1/M^0$  the time of flight of the photons.

In reflection geometry, the mean intensity  $M^0$  alone enables an accurate assessment of the transversal ( $x, y$ ) location of the fluorescent inclusion to be made but a poor depth value despite the tomographic acquisition. This is due to the fact that for a transrectal probe, the small distance between source and detectors leads to a reduced angle of view of the inclusion, which does not allow high-resolution  $z$ -axis determinations. To improve the determination of inclusion location in the  $z$  axis, the mean time of flight  $\langle t \rangle = M^1/M^0$  is used. Consider an infinite homogeneous medium. In such a case, the mean time of flight is simply related to the travel distance by  $\langle t \rangle = r/v$ , where  $v$  is a mean speed of light inside the tissues, and is given by:

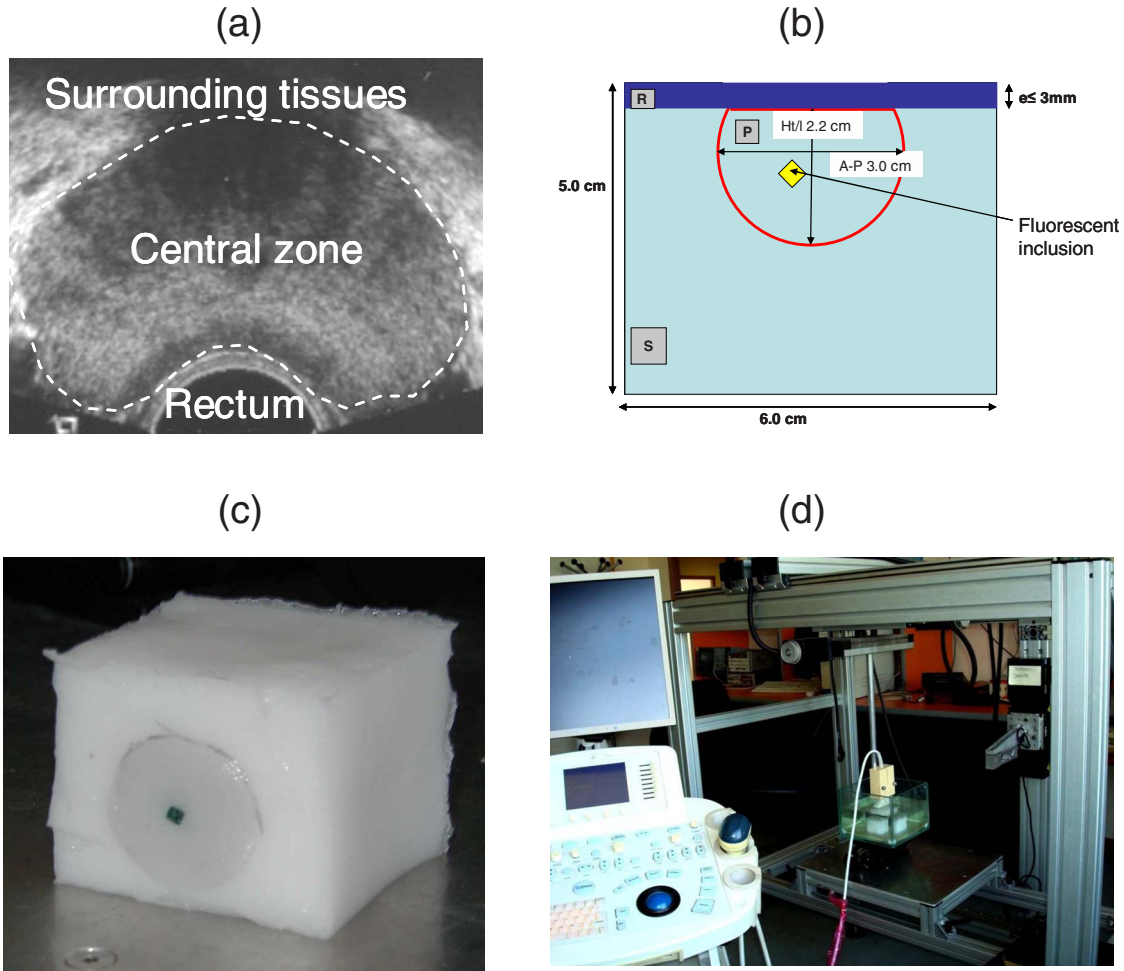


**Fig. 3** (a) Ultrasonic image of a healthy prostate. This image shows the three different kinds of tissues simulated by the phantom: rectum wall, central zone, and surrounding tissues. (b) Diagram of the prostate phantom [rectum wall (R), central zone (P), and surrounding tissues (S)]. (c) Photo of a previous version of the prostate phantom with the fluorescent inclusion (fluorescent glass) inserted 2 cm below the surface. (d) Photo of the prostate phantom placed inside the vat and being scanned by the Ultrasonic 500RP system.

$$v = 2 \frac{c}{n} \left[ \frac{\mu_a}{3(\mu_a + \mu'_s)} \right] = 2 \frac{c}{n} (\mu_a D)^{1/2}, \quad (3)$$

where  $c$  is the speed of light in vacuum,  $\mu_a$  is the absorption coefficient,  $D = [3(\mu_a + \mu'_s)]^{-1}$  is the diffusion, and  $\mu'_s$  is the reduced scattering coefficient. Considering the properties of the prostate phantom ( $\mu_a \approx 0.3 \text{ cm}^{-1}$  and  $\mu'_s \approx 7 \text{ cm}^{-1}$ ,  $n \approx 1.4$ ; Ref. 4), the mean speed of light inside the tissue is about  $5 \text{ cm} \cdot \text{ns}^{-1}$ . Given that the time step of the detection chain is 25 ps (one fraction of the detection time gate), the time of flight of the photons can be used to determine the depth of the inclusion with an uncertainty of 1 mm, which is sufficiently accurate for our application. Here, the forward model was computed using analytical formulas in an infinite medium.

#### 2.4 Accuracy of the Mean Time of Flight

Consider a temporal response acquired for a particular source–detector couple. This signal consists of  $n_i$  photon counts in temporal channels centred around the times  $t_i$ . From this signal, the total number of counts,  $N = \sum_i n_i$ , the mean time

of flight  $\langle t \rangle = (\sum_i n_i t_i / \sum_i n_i)$ , and the response width  $\Delta t = [\sum_i n_i (t_i - \langle t \rangle)^2 / N]^{1/2}$  are extracted. As the  $n_i$  values are corrupted by noise ( $n_i = \bar{n}_i + dn_i$ ),  $\langle t \rangle$  differs from its expected value by  $dt = \sum_i (\partial \langle t \rangle / \partial n_i) dn_i = \sum_i (t_i - \langle t \rangle) dn_i$ . As the  $n_i$  values are uncorrelated random variables and assuming that  $n_i$  follows a Poisson distribution, the variance of  $\langle t \rangle$  is  $\sigma(\langle t \rangle) = [\sum_i n_i (t_i - \langle t \rangle)^2]^{1/2} = (\Delta t / \sqrt{N})$ .

Therefore, the accuracy of the measurement can be as high as desired, provided the number of counts is high enough. For example, considering typical figures of a fluorescence half-life of 1 ns, a detection response of 500 ps, and a time transit widening of 1 ns, the response width will be 1.5 ns. Therefore, the time of flight measurement is accurate to within 25 ps with a 3600-count measurement, which is easily achievable.

#### 2.5 Prostate Mimicking Phantom

To validate this system, a tissue-mimicking phantom representative of the prostate tissues both on its optical (absorption  $\mu_a$  and diffusion  $\mu'_s$ ) and ultrasound properties was developed. This phantom represents the three different kinds of

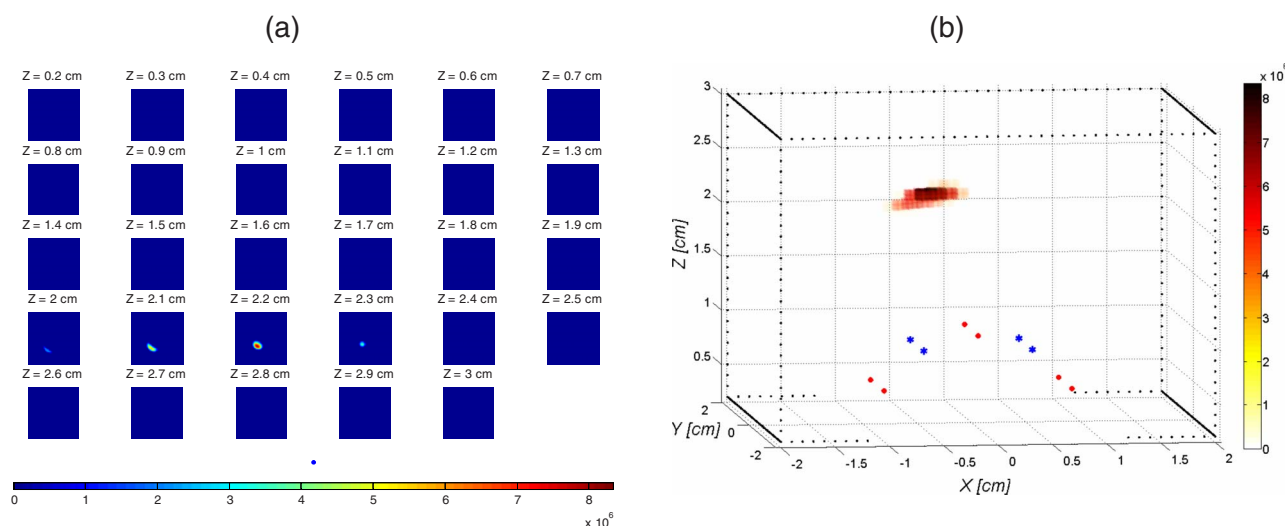


**Fig. 4** (a) Reconstruction results are represented by a series of slices in the  $xy$  plane, each image representing a slice at a given height  $z$  inside the phantom. (b) 3-D view of the previous reconstruction. Source (red dots) and detection (blue dots) fibers are also plotted. The reconstruction fluorescent inclusion was found at  $z=2.2$  cm. The difference between the real and reconstructed position of the inclusion ( $z=2$  cm) can be explained by the phantom surface deformation due to the probe. (Color online only.)

tissues comprising the prostate area: central zone, peripheral zone, and rectal tissue. This phantom is based on polyvinyl alcohol (PVA), silica, titanium dioxide, and ink. The dosage of the components was fine-tuned to fit the average prostate absorption and diffusion coefficient given by Svensson et al.<sup>4</sup> ( $\mu_a \approx 0.3 \text{ cm}^{-1}$ ,  $\mu'_s \approx 7 \text{ cm}^{-1}$ ). Silica powder was previously used in several studies<sup>12,13</sup> for adjusting acoustic scattering properties of tissue mimicking phantoms. A 5-mm cylinder was drilled and then filled with a 5- $\mu\text{l}$  capillary tube containing various concentrations of a fluorescent emulsion. This emulsion is based on Indocyanine Green (ICG) encapsulated in lipid nanodroplets. Its fluorescence yield (8.6%) is twice that of unmodified ICG (4.2%) and also has *in vivo* stealth properties.<sup>14</sup> The capillary tube was positioned inside the phantom, at a depth of 2 cm under its surface [Figs. 3(b) and 3(c)].

### 3 Results

Figure 4 shows the reconstructed fluorescent yield of a 1- $\mu\text{M}$  capillary tube obtained with the transrectal probe (six excitation and four detection fibers). Its  $x, y, z$  position was correctly recovered.

Location sensitivity of the system was determined by simulations. The time-dependent fluorescence signal due to an inclusion located at a depth of 1.2 cm was simulated by using an analytical propagation model and an exponential decay for the fluorophore. The background signal was taken to be leak-

**Table 1** Impact of the photonic noise on the theoretical accuracy of the  $x, y, z$  location of the inclusion.

	x axis	y axis	z axis
$3 \times$ standard deviation of the inclusion reconstructed position (mm)	0.6352	0.5122	0.2386

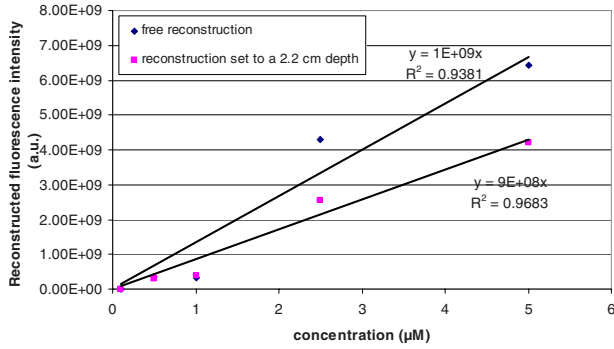
age from the excitation signal. The magnitude of this leak was chosen so that it fitted the experimental data. These two signals were convolved with a Gaussian impulse response function (IRF) of 500 ps FWHM. Photonic noise was added to the signal. The noise amplitude was chosen so that it had the same level as the noise of the experimental data. For each source position and each detector fiber, it corresponds to about 10,000 photons per acquisition (integral of the time-dependent distribution of the signal).

Table 1 shows the impact of the photonic noise on the theoretical accuracy of the  $x, y, z$  location of the inclusion. The standard deviation values obtained show a theoretical submillimetric resolution of the system. However, in clinical conditions, prostate tissue heterogeneities, fiber-tissue coupling efficiency, and rectum wall surface conditions may impair the accuracy of reconstruction.

This good theoretical resolution can be explained by the high dependence of time of flight on inclusion depth in reflection geometry. For instance, a depth difference of 1 mm will lead to a time of flight of 0.04 ns, which is compatible with the 25-ps steps measured with the experimental acquisition

**Table 2** Average location and intensity of the reconstructed fluorescence intensity.

Fluorophore concentration ( $\mu\text{M}$ )	x position (cm)	y position (cm)	z (cm)	Fluorescence intensity (a.u.)
0.1	-0.22	0.56	2.03	2.40E+06
0.5	-0.35	0.61	2.22	3.41E+08
1	-0.32	0.62	2.17	3.21E+08
2.5	-0.3	0.54	2.33	4.28E+09
5	-0.37	0.73	2.36	6.43E+09



**Fig. 5** Reconstructed fluorescence intensity as a function of the capillary tube concentration with a depth fixed at 2.2 cm.

chain. As a comparison, intensity measurements (such as those obtained by a continuous wave acquisition system) in a similar geometry would not be capable of achieving a resolution better than 1 cm, which is not sufficient for efficient

biopsy driving. It can therefore be concluded that time-resolved measurements are required to lower the rate of false negative biopsies, which is an important quality factor for prostate cancer diagnostic.

Probe linearity was tested through several acquisitions and reconstructions of capillary tubes containing various encapsulated ICG concentrations (0.1–0.5–1.0–2.5–5.0  $\mu\text{M}$ ). The system was able to detect and accurately locate all these inclusions. Table 2 shows the average location and intensity of the reconstructed fluorescence intensity.

The reconstructed fluorescence intensity was found to be closely correlated ( $R^2=0.94$ ) to the capillary tube concentration, as shown in Fig. 5. This correlation factor reaches  $R^2=0.97$  when the  $z$  position is fixed at 2.2 cm, which shows the influence of the reconstructed depth location on the recovered fluorescence intensity.

Figure 6 shows the time-dependent distribution of fluorescence and background signal from the different source-detector indexes (for a 1- $\mu\text{M}$  capillary tube). The ratio between signal and background noise before reconstruction

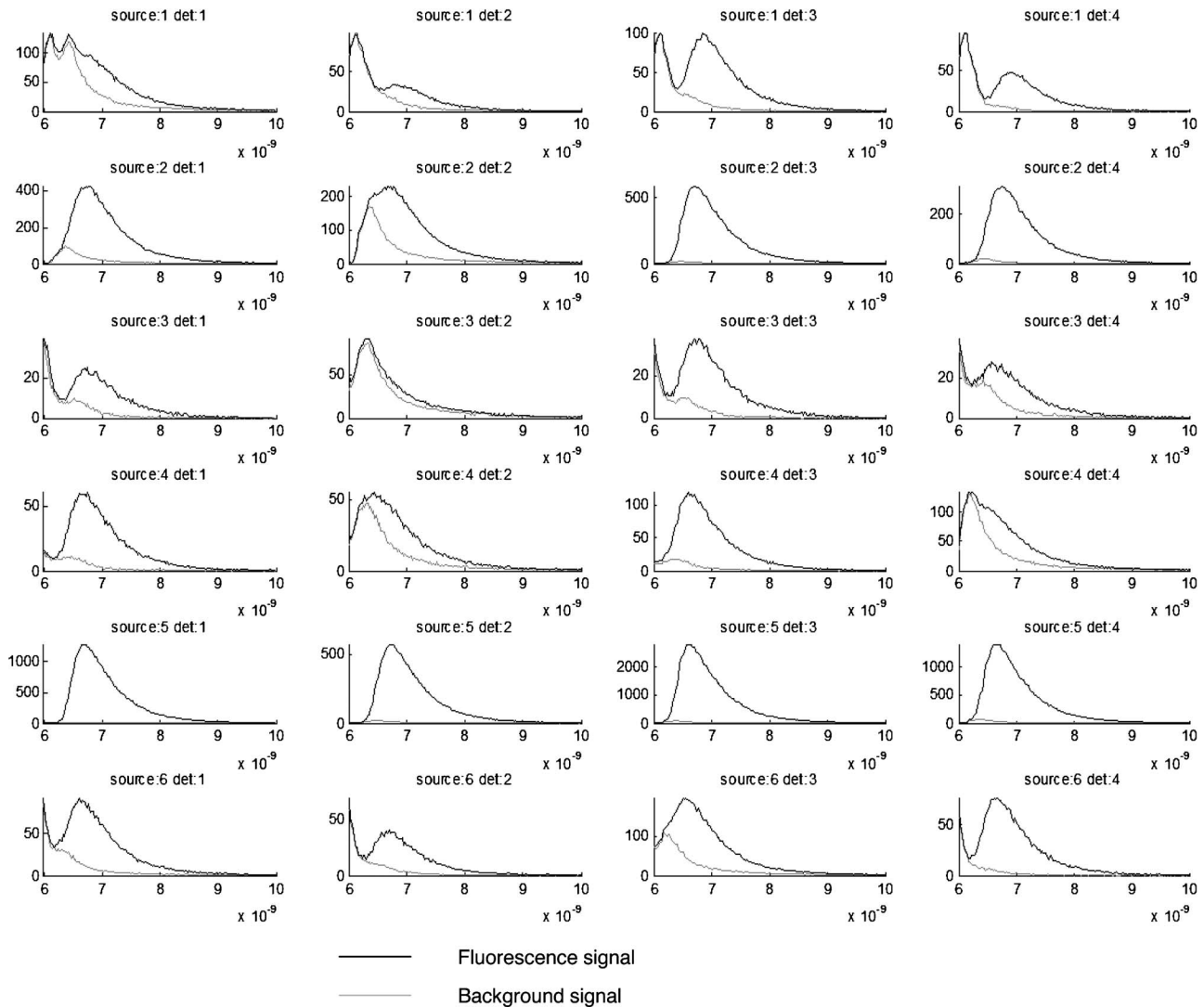


**Fig. 6** Time-dependent distribution of fluorescence (blue) and background (red) signal from the different source detector pairs (for a 1- $\mu\text{M}$  capillary tube). Source and detector indexes are shown on Fig. 2(a). (Color online only.)

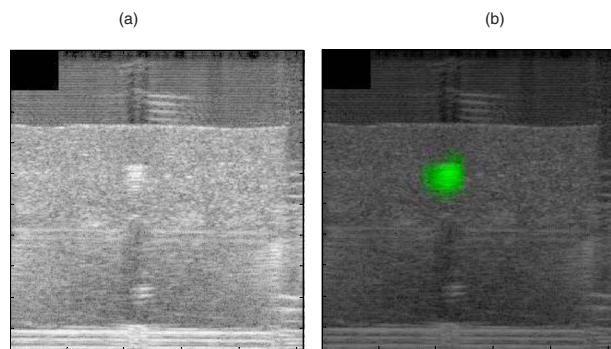


**Fig. 7** (a) This figure shows a central slice of the prostate phantom in the  $xz$  plane given by ultrasounds. This image shows the inclusion, which is more echogenous than the surrounding materials. The darker area under the inclusion corresponds to the shadow cone left by the inclusion. (b) Superimposition of the fluorescence map (in green) obtained after reconstruction on the ultrasound slice (gray scale). The high spatial heterogeneity between water and the phantom creates acoustic noise through multiple scattering known as pulse reverberations. The reverberations produce a tail added to the propagating pulse, and this tail is observed as additional noise at the top of the images. (Color online only.)

depends on the relative position of the excitation and emission fiber considered. The fluorescence signal decreases exponentially with the source–inclusion–detection distance, whereas the background signal depends only on the distance between source and detector. This explains why the best configuration was obtained for the source 5 and detector 3 [numbering is defined on Fig. 2(a)] with a signal to background ratio of 93. The least informative channel was the source 3 and detector 2 with a signal to background ratio of 0.2.

Experiments indicated that the current acquisition chain is able to detect the inclusion of  $0.1 \mu\text{M}$  down to a depth of 2.5 cm. To improve this detection limit and to decrease the overall acquisition time, it is planned to replace the current acquisition chain based on the HRI by four photomultiplier tubes connected to a 4-channel time-correlated single-photon counting (TCSPC) chain.

The reconstructed fluorescence map and the ultrasound image obtained with the bimodal auxiliary acquisition system described in Ref. 11 superimposed accurately [Figs. 7(a) and 7(b)], and this gives confidence in our ability to improve the sensitivity of endorectal prostate cancer diagnoses.

## 4 Conclusion

An integrated endorectal optical probe based on time-resolved FDOT was developed. It was designed to remain compatible with ultrasound measurements. Thanks to reconstruction based on an analysis of the time-dependent distribution of the fluorescence photons, it was possible to locate an inclusion at fixed depths inside a prostate-mimicking phantom. A  $0.1\text{-}\mu\text{M}$  capillary tube was reconstructed at a depth of 2.5 cm. The reconstructed fluorescence intensity was found to be closely correlated to the capillary tube concentration. One of the aims of future research will be to obtain better understanding of the

origin of the background signal. It will also be necessary to address the problem of reconstructing multiple tumors and the possible presence of heterogeneities in the prostate tissues.

## Acknowledgments

This work has been partly funded by the CARNOT Institute and the French Agence Nationale pour la Recherche (ANR). Dimensional information and ultrasonic images of prostate and endorectal probes were provided by Professor Nicolas Grenier of the Centre Hospitalier Universitaire de Bordeaux and by An Nguyen-Dinh (VERMON).

## References

1. I. N. Chiang, S. J. Chang, Y. S. Pu, K. H. Huang, H. J. Yu, and C. Y. Huang, "Major complications and associated risk factors of trans-rectal ultrasound guided prostate needle biopsy: a retrospective study of 1875 cases in Taiwan," *J. Formos Med. Assoc.* **106**(11), 929–934 (2007).
2. G. Xu, D. Piao, C. Musgrove, C. Bunting, and H. Dehghani, "Trans-rectal ultrasound-coupled near-infrared optical tomography of the prostate Part I: simulation," *Opt. Express* **16**, 17484–17504 (2008).
3. D. Piao, H. Xie, W. Zhang, J. S. Krasinski, G. Zhang, H. Dehghani, and B. W. Pogue, "Endoscopic, rapid near-infrared optical tomography," *Opt. Lett.* **31**(19), 2876–2878 (2006).
4. T. Svensson, S. Andersson-Engels, M. Einarsdóttir, and K. Svanberg, "In vivo optical characterization of human prostate tissue using near-infrared time-resolved spectroscopy," *J. Biomed. Opt.* **12**(1), 014022 (2007).
5. M. E. Eames, D. Piao, and H. Dehghani, "Source and detector fiber optimization for depth sensitivity in endoscopic near infrared tomography," in *Biomedical Optics (BIOMED)*, OSA Technical Digest (CD), A. Hierlemann, Ed., Paper BSuE30, Optical Society of America, New York (2008).
6. Z. Jiang, D. Piao, G. Xu, J. Ritchey, G. Holyoak, K. Bartels, C. Bunting, G. Slobodov, and J. Krasinski, "Trans-rectal ultrasound-coupled near-infrared optical tomography of the prostate Part II: experimental demonstration," *Opt. Express* **16**, 17505–17520 (2008).
7. A. Agarwal, S. W. Huang, M. O'Donnell, K. C. Day, M. Day, N. Kotov, and S. Ashkenazi, "Targeted gold nano-rod contrast agent for prostate cancer detection by photoacoustic imaging," *J. Appl. Phys.* **102**, 064701 (2007).
8. Y. Pu, W. B. Wang, B. B. Das, S. Achilefu, and R. R. Alfano, "Time-resolved fluorescence polarization dynamics and optical imaging of Cytate: a prostate cancer receptor-targeted contrast agent," *Appl. Opt.* **47**(13), 2281–2289 (2008).
9. A. Koenig, L. Hervé, V. Jossierand, M. Berger, J. Boutet, A. Da Silva, J.-M. Dinten, P. Peltié, J.-L. Coll, and P. Rizo, "In vivo mice lung tumor follow-up with fluorescence diffuse optical tomography," *J. Biomed. Opt.* **13**(1), 011008 (2008).
10. A. Corlu, R. Choe, T. Durduran, M. A. Rosen, M. Schweiger, S. R. Arridge, M. D. Schnall, and A. G. Yodh, "Three-dimensional in vivo fluorescence diffuse optical tomography of breast cancer in humans," *Opt. Express* **15**(11), 6696–6716 (2007).
11. J. Boutet, M. Debourdeau, L. Herve, L. Guyon, J. M. Dinten, and P. Rizo, "Advances in bi-modal optical and ultrasound detection of prostate cancer," in *Multimodal Biomedical Imaging IV*, San Jose, CA, F. S. Azar and X. Intes, Eds., *Proc. SPIE* **7171**, 71710E (2009).
12. C. L. de Korte, G. Pasterkamp, A. F. van Der Steen, H. A. Woutman, and N. Bom, "Characterization of plaque components with intravascular ultrasound elastography in human femoral and coronary arteries in vitro," *Circulation* **102**(6), 617–623 (2000).
13. L. K. Ryan and F. S. Foster, "Tissue equivalent vessel phantoms for intravascular ultrasound," *Ultrasound Med. Biol.* **23**(2), 261–273 (1997).
14. F. Navarro, M. Berger, M. Goutayer, S. Guillermet, V. Jossierand, and I. T. Noguees, "A novel indocyanine green nanoparticle probe for non-invasive fluorescence imaging in vivo," in *Proc. BIOS SPIE Photonics West*, San Jose, CA, S. Achilefu and R. Raghavachari, Eds., *Proc. SPIE* **7190**, 71900L (2009).